

PAPER • OPEN ACCESS

## Modular constructed metal-grid arrays—an alternative to silicon-based microplasma devices for catalytic applications

To cite this article: Sebastian Dzikowski *et al* 2020 *Plasma Sources Sci. Technol.* **29** 035028

View the [article online](#) for updates and enhancements.



**IOP | ebooks™**

Bringing together innovative digital publishing with leading authors from the global scientific community.

Start exploring the collection—download the first chapter of every title for free.

# Modular constructed metal-grid arrays—an alternative to silicon-based microplasma devices for catalytic applications

Sebastian Dzikowski<sup>1,3</sup> , Ronan Michaud<sup>2</sup> , Henrik Böttner<sup>1</sup>,  
Remi Dussart<sup>2</sup> , Marc Böke<sup>1</sup>  and Volker Schulz-von der Gathen<sup>1</sup> 

<sup>1</sup>Ruhr-University Bochum, Experimental Physics II, Universitätsstr. 150, 44801 Bochum, Germany

<sup>2</sup>GREMI, Université d'Orléans, 14 rue d'Issoudun, BP6744, 45067 Orléans, France

E-mail: [sebastian.dzikowski@rub.de](mailto:sebastian.dzikowski@rub.de)

Received 12 November 2019, revised 17 January 2020

Accepted for publication 30 January 2020

Published 19 March 2020



CrossMark

## Abstract

Here, we present a modular constructed metal-grid micro cavity plasma array as a flexible, robust, and simple alternative to micro-structured devices based on silicon. They show great potential for applications requiring large-area treatment, catalytic conversion or decomposition of volatile organic compounds. The metal-grid array is an easily assembled layered structure consisting of a metal grid, a dielectric foil and a magnet. The grid contains between hundreds and thousands of uniformly arranged cavities with a diameter of 150  $\mu\text{m}$ . The whole system is kept together by magnetic force. This also allows disassembling and exchange of the components independently. Typically, the arrays are operated close to atmospheric pressure with an alternating voltage of up to 1.4 kV peak-to-peak in the kHz range. For a first comparison with silicon-based configurations, the metal-grid array is examined from two different perspectives using phase-resolved imaging. The individual cavities show the same asymmetric discharge behaviour as in the silicon-based arrays. In addition, the expansion width of the discharge from the cavities could be measured. The same interaction between the cavities with the propagation of an ionization wave with velocities in the km/s range is observed as for the silicon-based devices. Thus, with respect to the most basic discharge properties, both configurations show the same behaviour, although they are different in structure and composition.

Keywords: phase-resolved imaging, atmospheric pressure plasmas, dielectric barrier discharge, plasma catalysis


## 1. Introduction

Micro-structured plasma discharges offer great potential for technical applications [1]. For example, they can be used for surface treatments [1] or for the decomposition of volatile organic compounds (VOC) [2]. Another field of application that is becoming a centre of interest is plasma catalysis [3].

<sup>3</sup> Author to whom any correspondence should be addressed.

Plasma catalysis can be realised in two different ways: firstly, in the so-called single-stage or in-plasma catalysis where the plasma and the catalyst are in direct contact. Due to the direct interaction between the plasma and the catalyst, the properties of the plasma and the catalyst such as the electric field or the morphology can influence one another. Secondly, in two-stage or post-plasma catalysis, the plasma is spatially separated from the catalyst [4]. For in-plasma catalysis some researchers have observed the formation of micro-discharges in pores in the catalyst where the increased electric field changes the electron energy distribution function (EEDF) [4, 5].

From a scientific and technical point of view, micro-discharges offer the advantage that geometric dimensions of the discharge can be defined and limited by the confining

 Original content from this work may be used under the terms of the [Creative Commons Attribution 4.0 licence](https://creativecommons.org/licenses/by/4.0/). Any further distribution of this work must maintain attribution to the author(s) and the title of the work, journal citation and DOI.

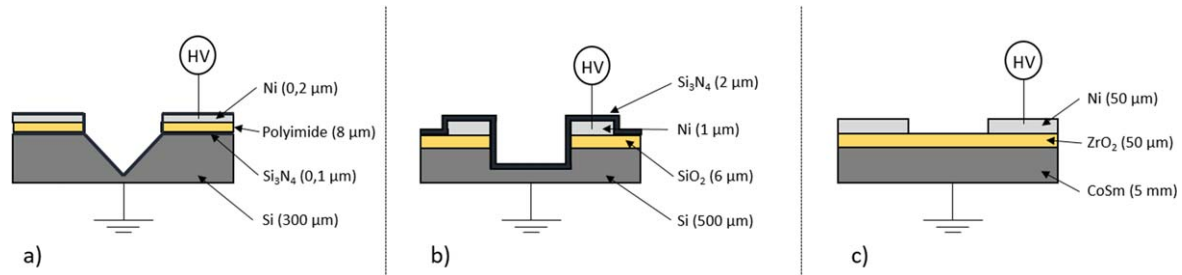


**Figure 1.** Schematics of silicon-based micro cavity plasma arrays (SBAs) with inverse pyramidal (a) and cylindrical (b) cavities and of the metal-grid micro cavity plasma array (MGA) (c).

cavity to the scale of about  $100\ \mu\text{m}$  [1]. In addition, a large number of these micro-discharges can be arranged uniformly in an array. Based on the applied micro-structure production techniques, an automatic reproducibility is enabled for the individual micro-discharges and arrangement on large areas into micro cavity plasma arrays (MCPA) [1, 6].

These configurations of microplasmas have already been introduced based on many materials; ceramics [7], photo-definable glass [8] and  $\text{Al}_2\text{O}_3/\text{Al}$  [9] structures have been processed. Another promising representative is silicon. The micro-structure technique allows one to incorporate a large number of functions in the micrometre- and nanometre-range in a controllable way [1]. The group of G Eden has developed silicon-based micro cavity plasma arrays (short: silicon-based arrays, SBA) [1, 10]. In this case, inverse pyramidal cavities were introduced into a silicon wafer by wet etching. These cavities are evenly arranged and have a base length of about  $100\ \mu\text{m}$ . A silicon nitride ( $\text{Si}_3\text{N}_4$ ) coating of the wafer in combination with a polyimide acts as a dielectric barrier to a nickel electrode. This nickel electrode is coated on the plane surface outside the cavities. Often another dielectric coating covers the whole cavity to increase the lifetime. In that case AC operation is required. The structure is illustrated in figure 1(a). A variant with cylindrical shaped cavities was developed and investigated by the group of R Dussart [11, 12]. A schematic sketch is shown in figure 1(b). In contrast to the first case, these cavities are ion etched, but the basic structure is the same. The silicon wafer typically is operated as a grounded electrode, with the nickel layer as the powered one.

Due to the AC operation, the emission is confined to time periods when the applied voltage reaches sufficient values for ignition. It was found that these emission phases can show self-pulsing, in which each pulse can be assigned to a wave propagation on the array. It was observed that not all cavities ignite at the same time, but a successive wave-like ignition occurs travelling along the cavity surface with velocities in the  $\text{km/s}$  range [13]. The number of pulses can be changed with voltage and frequency [14]. Depending on the polarity of the driven electrode, different emission structures can be observed for the individual cavity, which can be responsible for the formation of the ionization wave. The ignition and operation of a single inverse pyramidal cavity was numerically investigated by Kushner *et al* [15]. A first numerical attempt to describe the wave phenomenon was made in [16].

Unfortunately, this approach was just dealing with the negative voltage polarity while typically these devices are operated with an AC voltage waveform. However, this phenomenon is still not fully understood. An open question connected to wave propagation is the expansion out of the cavities. Observation by optical diagnostics is typically limited to the head-on direction. Grazing observation is usually hindered by shielding at the border of the devices to prevent arcing or by mounts and connectors. Thus, the actual expansion of the discharge out of the cavities cannot be investigated. Apart from this, different ignition characteristics could be observed for arrays with cavities of varying dimensions [17].

Apart from the open scientific questions and considering an application for plasma catalysis, SBA devices do not allow integration of a catalyst due to the complex manufacturing process. Detailed investigations on the plasma catalyst interaction are difficult too. A subsequent removal of the dielectric or the nickel grid for examination of changes caused by the discharge is also not possible. This can be important because it has been shown that the dielectric is exposed to a strong ion bombardment [12, 18].

To enable an enforcement of these investigations and applications, a metal-grid micro cavity plasma array (short: metal-grid array, MGA) device (see figure 1(c)) was developed and investigated showing long-term stability under laboratory conditions. The simple stacked device is constructed of exchangeable and demountable components such as a magnet, a dielectric sheet consisting of zirconium oxide ( $\text{ZrO}_2$ ) and a nickel grid with variable cavity dimensions in the range of  $100\ \mu\text{m}$ . A more detailed description of this device is given in section 2.1.

In order to further investigate the wave phenomenon observed on silicon-based arrays with the MGA, the following question naturally arises: are the different configurations comparable at all? For example, the configurations differ in geometry, dimensions, material selection and structure.

In this paper we compare silicon (SBA) and metal (MGA) based configurations with respect to the UI-characteristic, asymmetric discharge behaviour and ionization wave phenomena by using voltage and current probes and phase-resolved imaging (PRI). To support understanding of the wave propagation mechanism, measurements of the discharge expansion widths on the MGA that were previously not possible on SBA are presented.

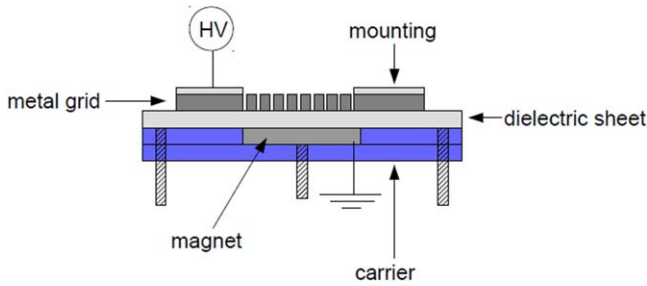


**Figure 2.** Schematic sketch of the metal-grid micro cavity plasma array (MGA).

## 2. Experimental configurations

### 2.1. Metal-grid array

In figure 2 a more detailed schematic sketch of a MGA is illustrated. The simple stacked configuration consists of a metal grid, a dielectric sheet and a magnet. The samarium-cobalt ( $\text{Sm}_2\text{Co}_{17}$ ) magnet serves as grounded counter electrode. It is inserted in a square acrylic glass carrier with an edge length of 40 mm and a height of 5 mm. The electrical connection to ground is attached to the metallic coating of the actual  $\text{Sm}_2\text{Co}_{17}$  magnet. Thin ceramic foils (KERAFOL) are used as a dielectric; 50  $\mu\text{m}$  thick zirconium oxide ( $\text{ZrO}_2$ , relative permittivity  $\epsilon_r \approx 27$ ) foils or 60  $\mu\text{m}$  thick aluminium oxide ( $\text{Al}_2\text{O}_3$ ,  $\epsilon_r \approx 9$ ) foils are available for this purpose. They cover the whole surface of the carrier. For the powered electrode (HV), a 50  $\mu\text{m}$  thick square metal sheet of nickel or stainless steel is used. In the middle of this sheet identical laser cut cylindrical cavities are arranged in a square pattern in an area of 1  $\text{cm}^2$ . Here, only experiments at cavities of 150  $\mu\text{m}$  diameter are described, but further cavity dimensions are available. Due to the magnetic property of the nickel grid, the sheet is pulled to the magnet. An additional 1 mm thick iron frame with an opening for the cavity structure completes this assembly. The frame ensures that all components are pushed together and all undefined movements of the thin sheets are suppressed. During the assembly, dust on the surface has to be prevented to allow a homogeneous close contact of the various sheets. Supporting pins allow the installation of the carrier to an adjustable mount. This configuration allows a handy exchange of dielectric sheets and metal grids.

**2.1.1. Operation conditions.** For the investigations presented here, the MGA is operated with pure helium as working gas in a pressure range between 200 mbar and 1000 mbar. In general, argon, nitrogen, oxygen, synthetic air and carbon dioxide have been added. Typical admixtures investigated up to now are in the 5 vol-% range. Due to the configuration of the array devices with an incorporated dielectric barrier, a repetitive centred bipolar triangular voltage waveform is applied to the metal grid of the micro cavity plasma array. This has the advantage that the excitation voltage slope stays constant within time periods of rising or falling voltage applied to the discharge. This allows one to simplify the

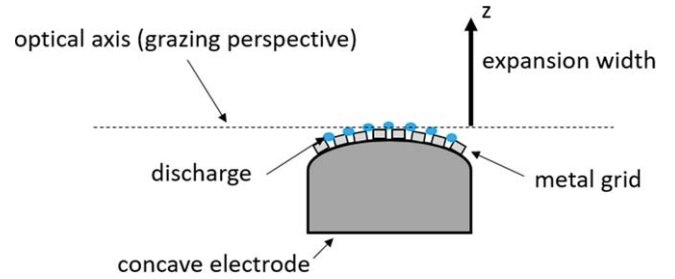


**Figure 3.** Schematic sketch of the setup for measuring the expansion width of the discharge. In this kind of setup the surface normal of a cavity line is orthogonal to the optical axis (grazing perspective).

interpretation of processes during those discharge phases [14]. The amplitude of the excitation voltage can be varied between 300 and 700 V in a frequency range between 5 and 15 kHz.

**2.1.2. Influence of magnetic field.** As explained in section 2.1, the grounded electrode is realised by a magnet; this raises the question of whether the discharge is influenced by that. The magnetic field strength  $B$  was measured on the surface of the magnet with a Gauss-meter (LakeShore-Model 421) and a corresponding probe (LakeShore-MMT-6J04-VH). The magnetic field has a strength of about 0.2 mT. A discharge is typically characterised as non-magnetized when the gyration radius  $r_g$  is greater than the mean free path  $\lambda_m$  [19].

$$r_g > \lambda_m \quad (1)$$

or

$$\frac{mv}{eB} > \frac{k_B T_{\text{gas}}}{p\sigma_{e/I}} \quad (2)$$

If we assume that the gas temperature  $T_{\text{gas}}$  is about 360 K [20], the electrons have a mean energy of about 2 eV and the total momentum transfer cross section between helium and an electron or a helium ion is about  $\sigma_e = 7 \cdot 10^{-20} \text{m}^2$  [21] and  $\sigma_I = 1 \cdot 10^{-18} \text{m}^2$  [22], we obtain a necessary magnetic field strength of about 22 T for the electrons and 230 T for ions at a pressure of 200 mbar. This means that significantly higher field strengths are necessary than that of the installed magnet. For higher pressures even higher field strengths are required. Therefore, the discharge is not influenced by the magnet.

**2.1.3. Concave MGA.** One advantage of the metal-grid design presented in section 2.1 is its flexible character. This allows the grid to be mounted on a concave counter electrode consisting of aluminium. In this case, the concave electrode has a curvature radius of 50 mm and is coated with a 30  $\mu\text{m}$  thick  $\text{Al}_2\text{O}_3$  layer and the metal grid is fixed on it. A sketch of the setup is shown in figure 3. In this configuration, it is possible to focus on just a few cavity lines in an orientation where the surface normal of the MGA is orthogonal to the optical axis (grazing perspective, see figure 3). This allows

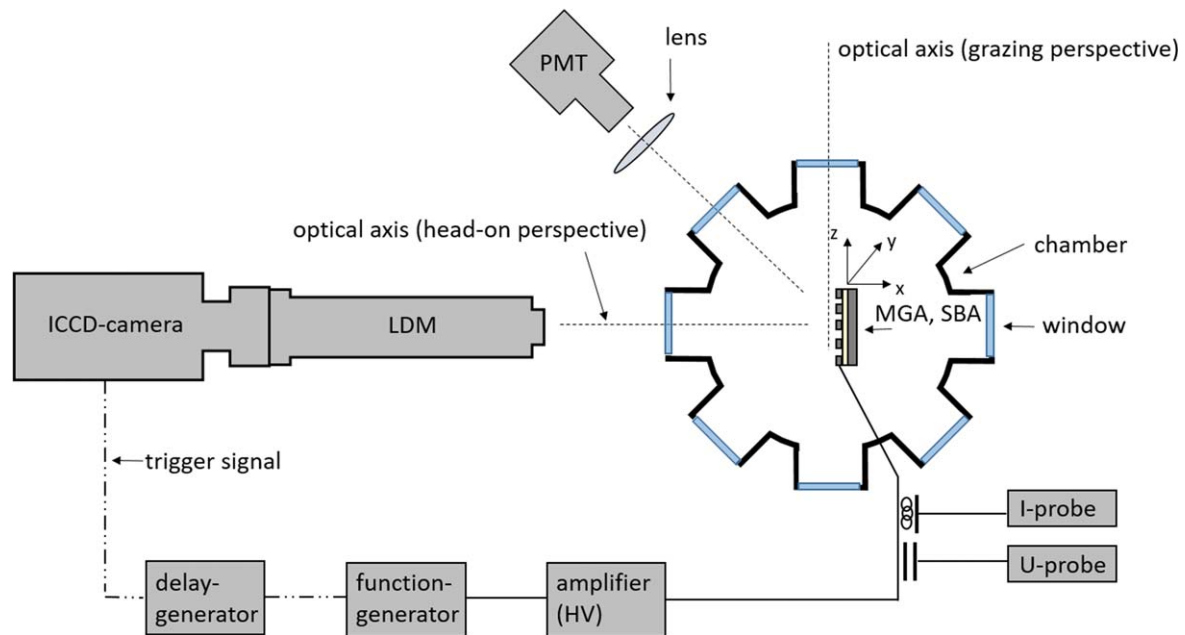


**Figure 4.** Schematic sketch of the used setup and diagnostic system. Grazing and head-on perspectives of the optical axis are used for different investigations of the array surfaces with the camera—long distance microscope (LDM) combination.

one to measure how far the discharge expands out of the cavities in the  $z$  direction as shown in figure 3.

The measurement of the so-called expansion width is difficult to design for the SBA. On the one hand, these arrays are not flexible and on the other hand, an isolation is usually attached around the cavity structure preventing optical access for this type of measurement.

## 2.2. Silicon-based arrays

This section briefly describes the SBA to provide a direct comparison and overview. Further information can be found in the respective literature [17, 23, 24].

SBAs with inverse pyramidal cavities are based on a  $300\ \mu\text{m}$  thick silicon wafer. The cavities are incorporated by a wet etching process. The cross section as shown in figure 1(a) is defined by the crystal axis of the wafer. The cavities are  $35\ \mu\text{m}$  deep and have a typical base area of about  $50 \times 50\ \mu\text{m}^2$ . A  $0.1\ \mu\text{m}$  thick silicon nitride ( $\text{Si}_3\text{N}_4$ ) layer is then applied to the entire surface using plasma-assisted gas phase deposition. An  $8\ \mu\text{m}$  thick polyimide layer on the plane surfaces separates the grounded silicon wafer from the high voltage driven nickel electrode. The nickel electrode has a thickness between  $0.12\ \mu\text{m}$  and  $0.2\ \mu\text{m}$  and is deposited on the polyimide by electron beam vaporization. Finally, the whole structure is covered again with  $\text{Si}_3\text{N}_4$  [23, 24].

An alternative to the inverse pyramidal cavities are cylindrical cavities. In this case, the silicon wafer has a thickness of  $500\ \mu\text{m}$  and serves also as a grounded electrode. This wafer is then covered with silicon oxide having a thickness of  $6\ \mu\text{m}$ . A sputter process is used to apply a  $10\ \text{nm}$  thick titanium layer and a  $100\ \text{nm}$  thick copper layer for better adhesion. Due to their minor size these two layers are not sketched in figure 1(b). Subsequently, a nickel layer is

deposited electro-chemically having a thickness of  $1\ \mu\text{m}$ . It serves as the driven electrode. Finally, the whole structure is covered by a  $2\ \mu\text{m}$  thick  $\text{Si}_3\text{N}_4$  layer by using plasma-assisted gas phase deposition again. By this method, it was possible to create arrays of  $10\ \mu\text{m}$  deep cavities with variable dimensions on a single silicon wafer [17].

Both the MGAs and the SBAs are referred to as micro cavity plasma arrays (MCPAs).

## 2.3. Diagnostic setup

The used experimental setup and the optical diagnostics are displayed in figure 4. One of the micro cavity plasma arrays (MCPA) described in the subsections above is operated in a vacuum chamber to ensure a defined gas atmosphere. The vacuum chamber can be pumped down to a pressure of  $2.0 \times 10^{-5}$  mbar by a turbo pump system (TMP, Pfeiffer TMU 520PC) to reduce impurities. In the case of helium a purity of 99.999% is used. The chamber is equipped with several quartz windows for optical access. For fine spatial adjustment the MCPA is fixed on a three-axis ( $x, y, z$ ) mounting stage (Mechonics MX-35) positioned in the centre of the vacuum chamber. This allows an orientation of the array's surface normal or parallel to the optical access. Feedthroughs are installed for the electrical contacting of the MCPA. A function generator (Tektronix AFG 3021B) delivers the voltage waveform. It is amplified by an electronic amplifier (HV, FM Electronic DCU 600-40 HF) to the high voltage range and finally leads to the MCPA.

## 2.4. Optical and electrical diagnostics

Optical investigations are performed in two different ways. For a spatially integrated recording of the discharge, the emission is imaged with a lens ( $f = 200\ \text{mm}$ ) on a photo-

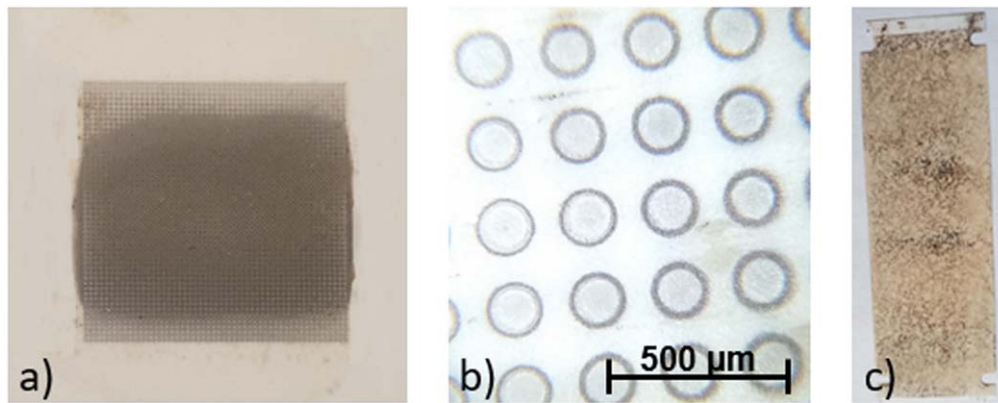


**Figure 5.** Photograph of (a) a dielectric sheet removed from below a nickel grid with  $150\ \mu\text{m}$  diameter holes after an eight month operation time and (b) an enlarged view of it. The contours of the cavity structure are clearly identified. First XPS measurements show that carbon is deposited on the used dielectric. Picture (c) shows a test dielectric sheet with sprayed  $\text{MnO}_2$  having a load of  $190\ \mu\text{g cm}^{-2}$ .

multiplier tube (PMT, Hamamatsu R3896). For spatial and phase-resolved imaging, the discharge is investigated by an intensified charge-coupled device (ICCD) camera (LaVision Picostar HR16) coupled to a long distance microscope (LDM, Questar QM 1) allowing a maximum resolution of about  $7\ \mu\text{m}$  per pixel. In the grazing perspective the optical axis of this system is oriented orthogonal to the surface normal of the respective array. In the head-on perspective the optical axis of this system is oriented parallel to the surface normal. For phase-resolved imaging (PRI) the ICCD camera is gated at a specific point in time (phase) within the repetitive period of the applied waveform. For the experiments presented here, the ICCD camera is operated with a typical gating time of  $200\ \text{ns}$  and an integration time of  $1\ \text{s}$ , i.e. integrating over a few thousand cycles. The phase shift of the recording is controlled by a delay generator (Stanford Research Systems DG535), which is triggered on the rising edge of the applied voltage from the function generator.

Outside the chamber, voltage (Tektronix P6015A) and current (Tektronix P6021) probes are connected to the electrical wiring of the MCPA. The signals are recorded via an oscilloscope (Hewlett-Packard HP 54540C,  $500\ \text{MHz}$  bandwidth) and subsequently stored on a computer.

### 3. Results and discussions

#### 3.1. Lifetime and exchange of components

The MGA reaches a minimum lifetime of about 400 operation hours. The measurements presented here were done with just a single device.

As a proof of the general feasibility of the concept for catalyst investigations, the MGA was disassembled into its individual components after been taken out of operation, investigated and subsequently reassembled. Figure 5 shows photographs of the  $\text{ZrO}_2$  dielectric. A dielectric removed after operation is displayed in figure 5(a). A black layer was formed within the cavity structure. Surface analysis was used to investigate changes on the dielectric. First X-ray photoelectron spectroscopy (XPS) measurements show that the

black structure is carbon probably formed during operation with  $\text{CO}_2$  admixture. In figure 5(b), an enlarged picture of the dielectric is shown recorded with an optical microscope. The contours of the cavity structure are recognizable. In addition to the strong deposit at the edges of the individual cavities, a slight coating within the contours can also be seen.

It is also possible to incorporate a dielectric that is previously coated with a catalyst shown in 5(c). In a first attempt, a load of about  $190\ \mu\text{g cm}^{-2}$  manganese oxide ( $\text{MnO}_2$ ) was spray coated on the  $\text{ZrO}_2$  sheet. This allows the investigation of the interaction between the micro-structured discharge and a catalyst. The subsequent installation and commissioning of the MGA was carried out successfully.

#### 3.2. UI-characteristic

In order to obtain a first comparison between the MGA and the SBA with inverse pyramidal cavities the current–voltage behaviour was investigated for similar values of voltage amplitude, frequency and pressure. Considering the combination of a multitude of individual cavities into an array the integrating properties of these measurements limit their informative value. Nevertheless, the UI diagnostic provides first valuable information for a comparison between the array configurations.

Figure 6 shows the characteristics of the two devices at different voltages. The applied voltage waveform (black profiles) has a frequency of  $10\ \text{kHz}$  and the pressure is  $500\ \text{mbar}$  in helium. The upper row of graphs show the behaviour of the MGA at  $330\ \text{V}$  6(a) and  $400\ \text{V}$  6(b). The MGA contains  $36 \times 36$  cavities with a diameter of  $150\ \mu\text{m}$ . The lower row shows the behaviour of an SBA at  $350\ \text{V}$  6(c) and  $390\ \text{V}$  6(d). The cavity structure of the SBA consists of  $50 \times 50$  cavities having a base length of  $100\ \mu\text{m}$  and an inter-cavity distance of  $100\ \mu\text{m}$ .

Since the array devices investigated here are constructed like capacitors, rectangular current signals are observed corresponding to the displacement current (red profile) for the applied triangular voltage waveform. When the ignition voltage of the discharge is reached, an additional discharge current can be observed. This takes place in the positive half

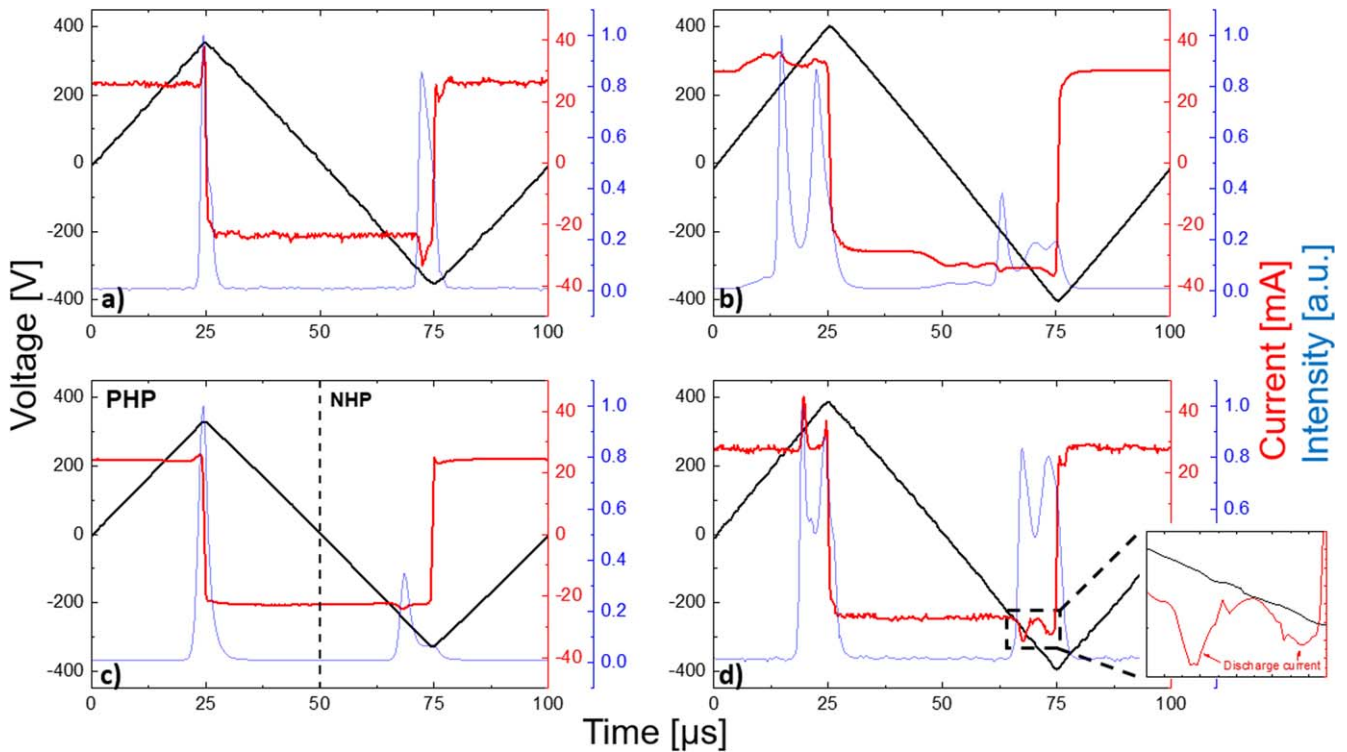


**Figure 6.** Temporal evolution of excitation voltage (black), current (red) and intensity (blue) for the MGA and SBA. The first row presents the characteristics of the MGA at excitation voltage amplitudes of (a) 330 V and (b) 400 V. The second row shows the characteristic of the SBA with voltage amplitudes of (a) 350 V and (b) 390 V.

period (PHP,  $U > 0$  V) as well as in the negative one (NHP,  $U < 0$  V) shortly before the voltage reversal. Since the discharge current ( $\lesssim 5$  mA) is much smaller in comparison to the displacement current (about 25 mA) it is hardly visible on the full scale graphs. Hence the discharge current of the NHP in figure 6(d) is illustrated enlarged (black dashed box) in the insert. At the same time as the discharge current, emission can be detected with the PMT (blue profiles).

An increase in voltage leads to an increase in the number of pulses occurring [14]. In the left column of figure 6 one can see only one emission and one current pulse for each half period. With a small increase of the voltage shown in the right column two pulses can be detected. During discharge pulses, spatial and surface charge centres are formed, which compensate the applied electric field. Therefore, a further discharge pulse can only be achieved by increasing the electrical voltage.

In the case of a frequency variation, however, an opposite behaviour is observed. While for the SBA the number of discharge pulses decreases with higher frequency [14], it increases for the MGA. For the SBA it was observed that the first pulse occurs at later ignition times (higher voltages) with higher frequency due to increasing surface charges. Therefore, the time between the first pulse and the reversal point gets smaller and fewer pulses can occur. However, the MGA show that the first pulse occurs earlier with higher frequency. So, the time to the vertex of the applied voltage allows more pulses. Due to the metallic structure the explanation based on surface charges fails. Possible processes based on residuals in

the volume reducing the ignition voltage will be part of further research.

As already observed for the SBA [12, 14], the intensity of the emission is greater in the PHP than in the NHP. This is due to the asymmetric behaviour discussed in section 3.3.

The MGA shows a discharge current of approximately 8 mA at an amplitude of 400 V. With the assumption that this current flows over the cavity base areas, a current density of about  $36 \text{ mA cm}^{-2}$  and a power density of about  $3 \text{ kW cm}^{-3}$  are achieved. For the SBA a current of approximately 18 mA is achieved, which results in a current density of approximately  $70 \text{ mA cm}^{-2}$  and a power density of  $24 \text{ kW cm}^{-3}$  for the above cavity structure. Both current densities are in the same order of magnitude and can be assigned to the atmospheric pressure glow discharge (APGD) [25].

In summary, it can be stated that both configurations show similar temporal behaviour in current and emission by applying the same excitation. The MGA and SBA can be assigned to the same discharge mode despite their different design.

### 3.3. Asymmetric discharge behaviour

Due to the dielectric barrier, the MCPA has to be operated with a bipolar voltage waveform. Different emission structures are recorded for the positive and negative half periods. This is illustrated in figure 7 where spectrally integrated phase-resolved images are shown. The images in the left and right columns correspond to recording in the positive (PHP) and negative (NHP) half period of the excitation, respectively.

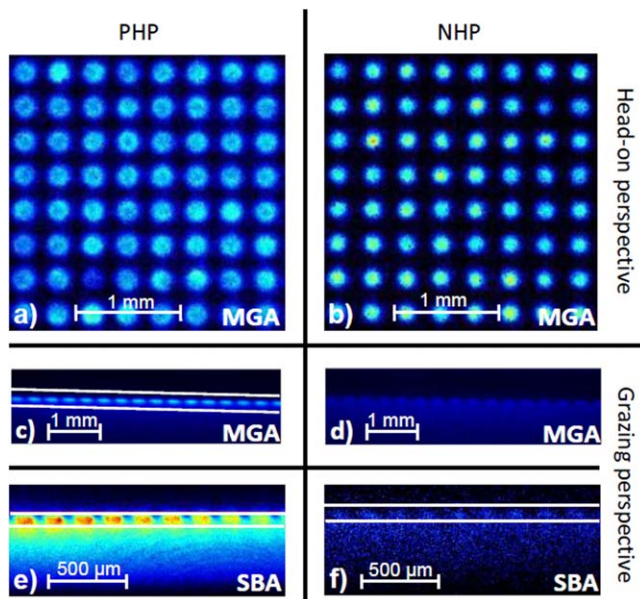


**Figure 7.** Spectrally integrated phase-resolved images for the PHP and NHP of the MGA and SBA at maximum intensity. The columns indicate the respective half period, the rows the perspective of the recording. The MGA is shown in the head-on perspective in image (a) and (b) and in the grazing perspective (c) and (d) operating at an amplitude of 300 V at 10 kHz. The SBA is shown in the grazing perspective in image (e) and (f). The white lines frame the cavity row. High emission intensity is displayed by bright and red colours, low intensity by dark and blue colours.

The images are taken with an integration time of 200 ns in pure helium at 200 mbar. The applied voltage is about 300 V at 10 kHz. In the first row (figure 7(a) and (b)) images recorded in the head-on perspective are presented where the ICCD camera looks directly on the cavity structure. Thus, the discharge distribution across the array surface becomes visible.

During the PHP, the discharge is mainly formed on a ring close to the cavities' edges inside (figure 7(a)). In the opposite phase (NHP) the discharge is located more centrally in the cavities (figure 7(b)). Due to the selected resolution the structure cannot be further resolved. This kind of asymmetry is also ascertained for SBA although structure and size are different. We found that it is not significant whether the formed cavities or trenches [17] engraved in the silicon wafer are cylindrical [26] or pyramidal [14].

In the case of SBA the radial emission profile was investigated for a single cavity on a wafer in [26]. The camera looked directly at the single cavity, comparable to the head-on perspective in figure 7. It was found that at higher pressures the emission is more pronounced at the edges of the cavity. For the NHP, with a 150  $\mu\text{m}$  large cavity, the emission structure changed from a bell-shaped structure with increasing pressure to a more ring-like structure. In the PHP the emission pattern of the discharge moves 70  $\mu\text{m}$  from the outside to the inside of the edge by increasing the pressure from 500 to 700 mbar. The largest applied electric field prevails there (comparable to [15] for SBA), allowing the electrons to be accelerated until excitation. The strong emission located at the

edge was correlated to the strong electric field and is probably responsible for the destruction of the SBA. The produced ions are accelerated along the edge towards the dielectric and damage it. After breaking through the dielectric coating, a high current discharge occurs, which leads to destruction of the device [18]. This correlates with the observations in figure 5(b), where a stronger coating on the dielectric can be seen at the cavity edges.

These observations for the MGA support the similar discharge mechanisms as previously considered on the SBA. When the grid is positively charged, the electrons are accelerated freely outwards due to the strong electric field along the edges and an avalanche is built up. In the NHP, however, the electrons are accelerated inwards and the discharge occurs there [14, 17]. Since the electrons are collected in the cavity, they reach lower energies on average than in the PHP. This means that fewer particles can be excited and consequently the intensity is lower as already mentioned in 3.2.

The MGA and SBA show very similar asymmetric emission structure in both half periods. So the basic physical processes seem to be the same. It also does not matter whether the cavities are engraved in the form of round holes, inverse pyramids or trenches.

#### 3.4. Discharge expansion

As already mentioned in section 2.1.3, one advantage of metal grids is their flexibility. Observation (in grazing orientation) of the range of the discharge emission expanding out of the cavities in the normal direction can be investigated with the camera. The middle row in figure 7 shows phase-resolved images of the MGA in the grazing perspective where the camera only focuses on just one cavity row in both half periods. The operation parameters are the same as in the head-on recorded images. The discharge clearly expands outside the cavities in the PHP (figure 7(c)). In the NHP (figure 7(d)) there is almost no emission detectable outside, which means that the discharge exists mainly inside the cavities.

The same result is also observed under only slightly different conditions for the SBA with inverse pyramidal cavities. In this case, the SBA operated at atmospheric pressure with argon with 20 kHz. Due to the isolation around the cavity structure, no exact parallel alignment of the optical axis to the cavity surface can be achieved. The camera is aligned obliquely to the SBA. However, in the PHP the discharge expands outside the cavities (figure 7(e)). In the NHP emission is hardly noticeable (figure 7(f)).

As the discharge in the PHP expands out of the cavities, the expansion width of the emission can be determined. The expansion width of the emission is here defined as the distance from the array surface at which the emission intensity has dropped to its  $1/e$  value. To obtain a high signal-to-noise ratio, the values were always recorded at the time of maximum intensity. Figure 8 shows the expansion width as a function of pressure for the MGA. Figure 8 demonstrates that the expansion width decreases with increasing pressure. At a pressure of 300 mbar the expansion is about 90  $\mu\text{m}$  whereas close to atmospheric pressure it is restricted to only 50  $\mu\text{m}$



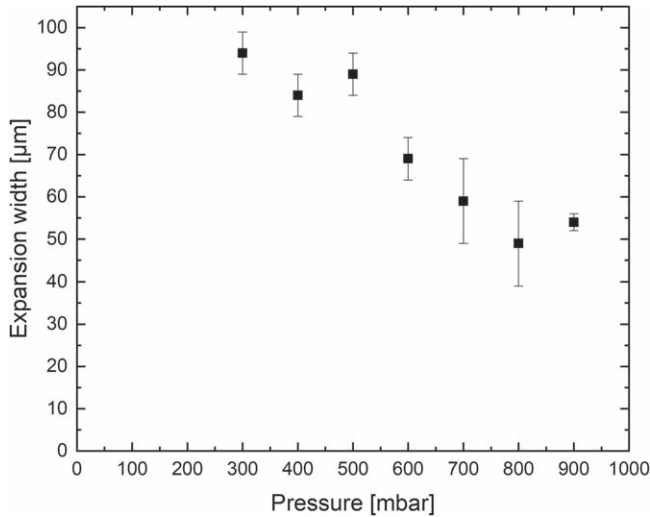


**Figure 8.** Expansion width depending on the pressure for the curved electrode configuration in the PHP. The device is excited by a triangular voltage waveform with an amplitude of 300 V at 10 kHz in helium. The  $36 \times 36$  cavities have a diameter of  $150 \mu\text{m}$ . The pressure is varied in the range between 300 and 900 mbar. For estimation of the expansion width, phase-resolved images are analysed as presented in figure 7 (middle row; grazing perspective).

away from the top of the array. The expansion widths are mean values calculated by averaging the width of all cavities of a single row over different rows that are brought into focus by turning the array. The standard deviation of this averaging is shown by the error bars. Relating the expansion width directly to the free path length  $\lambda_m$  of the electrons is probably oversimplifying. The complex interaction was simulated for the SBA having inverted pyramidal cavities in [15]. It is shown that the expansion of the electrons decreases and the discharge gets more confined with increasing pressure. One way to still achieve excitation is a stronger applied electric field.

These observations support the simplifying hypothesis (see section 3.3) that describes the radial propagation of the electrons in the discharge that excite the neutral gas particles above and outside the cavity in the PHP so that the ring-like emission structure is created.

### 3.5. Wave character

A major phenomenon shown by the SBAs is the non-simultaneous ignition of all the cavities. Instead, single cavities are first ignited. Subsequently, transfer of the emission into neighbouring cavities can be observed along the cavity surface [14, 17, 27]. The origin of this wave-like mechanism has not been understood yet.

Figure 9 shows phase-resolved detailed images of the discharge during the PHP for an MGA. The operating conditions are the same as in section 3.3. The time stamp refers to the ignition of a single pulse within the discharge. Since the gate is 200 ns wide, emission is already detected at the time stamp of 0 ns. In these images, the wave ignites preferably at the bottom left and moves within the excitation pulse to the top right of the cavity structure. This results in a total pulse

duration of approximately  $1.6 \mu\text{s}$ . It has to be noted that the actual pattern of the wave is different for any array and is probably dependent on small variations introduced during the production. This is also reflected in the NHP (not shown here). For the array described here, the discharge ignites at several positions in NHP so that several waves start to expand concentrically across the array structure, while observing only one starting point in the PHP. This hinders in many cases an unambiguous definition of the direction of the wave. However, it is interesting to note that the wave velocities are almost the same in both half periods. This is discussed in section 3.6.

Two possible mechanisms have been discussed to understand this wave propagation in [28]. The first of the two important mechanisms is connected with the production of photoelectrons. By the discharge in the primarily ignited cavities (here, bottom left) photons are emitted that interact with the surrounding cavities. Photoelectrons are released and can create an electron avalanche in these cavities. The second mechanism is the production of secondary electrons by ion impacts. In the NHP ions are accelerated out of the cavities and hit the dielectric surface. Afterwards, secondary electrons also create an avalanche in the surrounding cavities and the wave is maintained in such a way.

Considering the still not completely understood wave propagation, it is interesting to note that wave propagation is observed for all configurations (MGA, SBA) although basic geometric structures (shape of cavities, distances) and cavity surface properties are dissimilar. This already changes two basic physical properties that could play an important role, namely conductivity and different secondary electron emission coefficients.

Firstly, in the case of the MGA, the grid is metallic and not coated as the silicon-based configurations. Electrons as well as ions can disappear or be neutralised at the grid in the respective phases. Thus, the grid represents a charge carrier sink and charge carriers cannot remain on the dielectric layer as for the SBA.

Secondly, different materials are characterised by different secondary electron coefficients  $\gamma_{\text{see}}$ . In case of  $\text{Si}_3\text{N}_4$  the coefficient is 0.15, whereas for nickel a value can be estimated based on the following empirical formula [29]

$$\gamma_{\text{see}} = 0.032 \cdot (0,78\epsilon_{\text{ion}} - 2\epsilon_{\text{wf}}) \quad (3)$$

Here,  $\epsilon_{\text{ion}}$  is the ionization energy of the species colliding on the nickel surface. Due to the operation in helium, these ions collide mostly with the surface. The ionization energy is 24.587 eV. The work function  $\epsilon_{\text{wf}}$  of the nickel electrode is about 5.15 eV. Finally, a  $\gamma_{\text{see}}$  for nickel can be estimated to be 0.284, which is about 90% higher than for  $\text{Si}_3\text{N}_4$ .

In addition, wave propagation cannot be dependent on the applied electric field line configuration. In the case of SBA having inverse pyramidal cavities, one would expect a slightly different electrical field line configuration than in the case of cylindrical cavities. While in cylindrical cavities the electric field is strongest along the lower edges at the bottom of the cavity, in pyramidal cavities it is strongest at the tip and at the sides of the pyramidal structure.

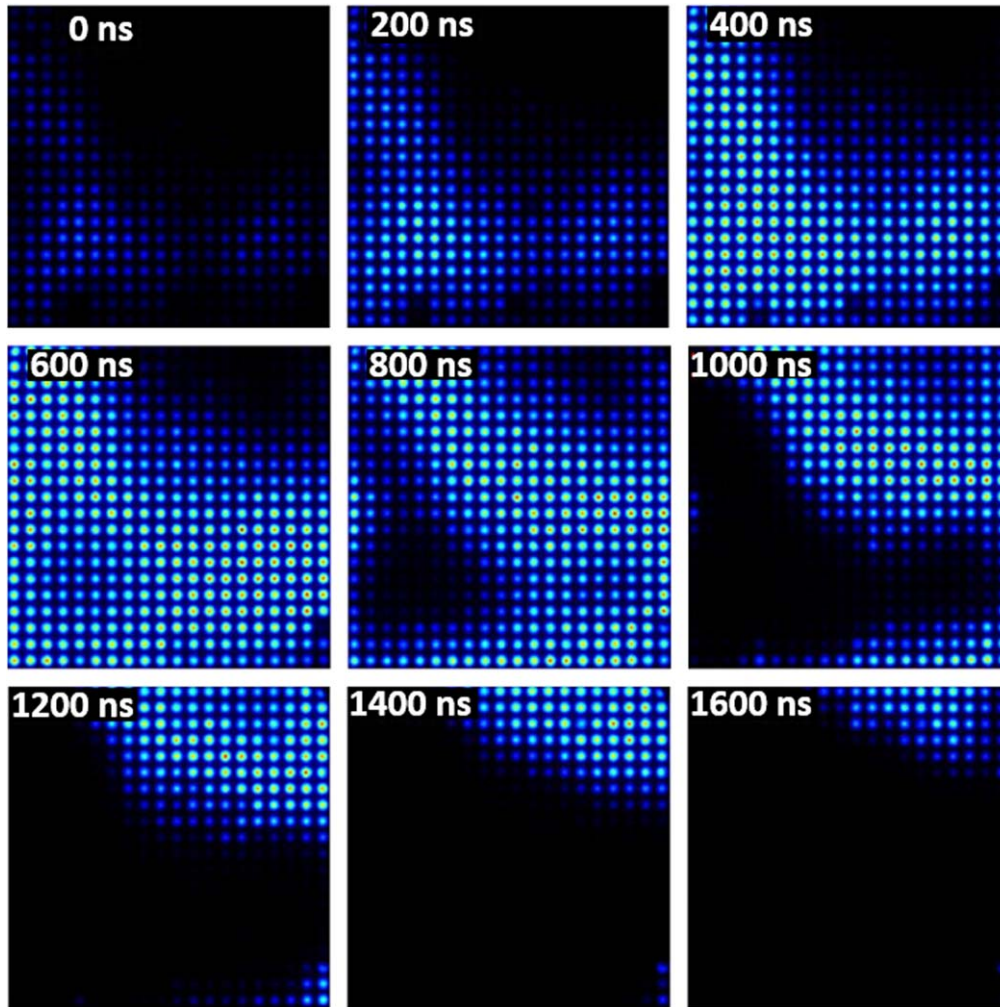


**Figure 9.** Phase-resolved images of the discharge pulse in the PHP with a time resolution of 200 ns. The spectrally integrated images, recorded with an integration time of 1 s by using the ICCD camera, show the ionization/excitation wave propagating across the array surface. Here, a triangular voltage waveform of 400 V at 10 kHz is applied in a helium atmosphere at 450 mbar. The  $36 \times 36$  cavities have a diameter of  $150 \mu\text{m}$ . The time stamp in each image refers to the delayed trigger signal for the camera. The time stamp at 0 ns refers to the ignition within the pulse. Since the gate is 200 ns wide, emission is already detected at 0 ns.

However, the process of photoelectron emission is questionable with respect to wave propagation in the NHP. There, hardly any visible emission could be observed outside the cavities, so this mechanism can only be dominant in the PHP. On the other hand, the process of secondary electrons by ions is then inconsistent, since in this case the ions move into the cavities.

In summary, it can be stated that wave propagation can also be observed for the MGA, but the mechanisms discussed in [28] can just be confirmed partially in the respective half periods. Since the spatial expansion during the pulse duration of the wave (figure 9) is known from the uniformly arranged cavities, the wave velocity can be estimated. The velocities are discussed in the next section.

### 3.6. Wave velocity

Figure 10 shows the wave velocity as a function of the pressure between 300 and 600 mbar for a MGA. The wave propagation is assumed to be a uniform motion. For the

estimation of the velocity, two random cavities were selected, whose distance can be determined by the given cavity structure. The time at which the intensity in the selected cavities has reached the maximum value can be determined with the camera. The displayed values result from averaging over 10 different cavity pairs. The error bars represent the sum of the stochastic and systematic uncertainties, which increases with higher pressure due to small intensities. For a better overview, not all error bars are shown.

The velocities increase more or less linearly from about  $1.0$  to  $2.0 \text{ km s}^{-1}$  for both polarities. This is in reasonable agreement with experimental measurements from the SBA, where velocities between  $3$  and  $6 \text{ km s}^{-1}$  were measured [13]. They are about 10 times smaller than in the simulation for SBA [28], where the measured velocities would be reached only in the absence of photoelectrons.

This allows one to come to two conclusions.

Firstly, the velocities are within errors almost the same for both half periods. This allows one to assume that the responsible processes must be the same in both half periods.

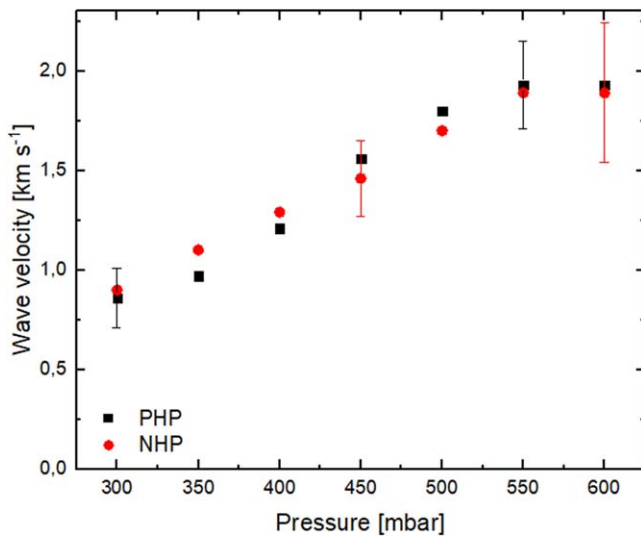


**Figure 10.** Wave velocity for a MGA depending on the gas pressure in pure helium. The applied bipolar triangular voltage waveform has an amplitude of 400 V at 10 kHz. The  $36 \times 36$  cavities have a diameter of  $150 \mu\text{m}$  and a centre-to-centre spacing of  $300 \mu\text{m}$ .

Thus, the secondary electron emission, which is described in the simulation [28] as an essential mechanism, must be caused by photons as well as by ions. However, as discussed in section 3.5, only in the PHP does the emission take place outside the cavities, so only in the PHP can secondary electrons be generated by photons in adjacent cavities. Secondary electrons by ions are only possible in the NHP because they are accelerated outside the cavities. This leads us to the hypothesis that both discussed processes are not dominant for wave propagation.

The second observation is that the velocities increase (within the errors) linearly with increasing pressure. This is interesting, because with higher pressure species-based processes like diffusion and drift between the cavities decrease due to the increasing number of collisions and therefore cannot support wave propagation.

Since we can exclude most of the physical processes as an explanation for the wave propagation another process that is pressure dependent for all kinds of devices must be found. One possibility would be to couple the plasma properties of the cavities with the electrical circuitry of the device.

In short, any array consists of a planar distributed resistor interrupted by capacitors, i.e. the cavities. The capacitance of the capacitors are pressure- and discharge-dependent.

To simplify a step further, a two-dimensional electrical equivalent network of discrete elements interconnected resistors and capacitors might be used to explain the wave propagation occurring in all the investigated configurations (SBA, MGA). In this RC-network each cavity of the array can be considered as a capacitor connected in parallel to the adjacent ones by resistances resulting from the surface resistance of the nickel grid. The distance between the nickel grid and the dielectric is not equal over the entire surface. Therefore, the ignition condition is the most suitable for one cavity. When the required voltage is reached, the initial discharge ignites preferably in this cavity and afterwards a

charge distribution is created, causing the voltage to drop over this cavity. This voltage drop results in currents through the resistors connected with the neighbouring cavities. Due to this current an additional voltage is induced in those capacitances that results in the ignition of the cavities. This is compensated by electrons from further capacitances that are further away and not ignited yet. This process is repeated until the last capacitance is reached, which is supplied directly from the power supply.

Due to the higher pressure the mean free path becomes smaller not only between the cavities, but also within the cavities. As a result the drift velocity of the charge carriers decreases and the charge distribution develops more slowly. Since the voltage drop is thus smaller, the adjacent capacitances have to compensate for fewer charge carriers in the ignited cavity and the ignition voltage is thus reached faster. The wave finally spreads faster.

One way to validate this described network is to investigate a time response after an impulse by means of software used in electrical engineering (e.g. PSpice), comparable to [30]. These networks show a time delay in impulse response between the different elements (capacitors, resistances) that would correspond to our wave propagation after the initial ignited cavity (impulse).

#### 4. Conclusion

In this work a metal-grid micro discharge array is introduced, investigated and compared to silicon-based devices. In a first step, it could be shown that the metal-grid array shows the same behaviour with respect to the current–voltage characteristics as compared to those that are silicon-based.

A characteristic that has been previously demonstrated in all SBAs is the asymmetric discharge expansion. The MGA also shows this behaviour and, due to its flexible structure, allows one to demonstrate that the discharge clearly prevails inside and outside the cavities in the respective periods as proposed in simple physical pictures.

PRI also made it possible to estimate the ionization wave velocities also occurring in the MGA. The velocities observed here are in the km/s range and are almost identical for both half periods. Compared to the SBA, the velocities are lower by a factor of about 10. Due to this fact and the clearly expanding discharge in the PHP, one can assume that the effect of photoionization cannot be the dominant one. An electrical circuit equivalent may explain the wave propagation, being compatible with the structural differences of the three investigated configurations and the pressure dependency of the propagating velocity. Further experimental and theoretical investigations are necessary to prove this hypothesis.

For the most general discharge characteristics of MGA and SBA, the different structure and the different material composition of the components do not seem to play a role.

Therefore, both configurations are comparable in their general observations, so that further insights into the wave phenomenon may also be transferred to the SBA.

Concerning applications, the potential of the concept for the investigation of the interaction between catalyst and plasma could be demonstrated. Furthermore, the observed asymmetry can be used favourably in relation to plasma catalysis. While in the positive phase the discharge preferably takes place outside the cavities, the catalyst can interact with the species produced in the discharge. The NHP follows in order to refresh or clean the catalyst.

## Acknowledgments

This work has been supported by the German Research Foundation (DFG) within project A6 of the collaborative research centre SFB 1316 ‘Transient atmospheric plasmas—from plasmas to liquids to solid’ and by the DAAD and the French Foreign Ministry within the PROCOPE project 57 134 635 ‘CoSi2Me’. We gratefully acknowledge the support by G Eden and his group at UIUC in supplying us with silicon-based arrays of inverted pyramidal configuration. We would also like to acknowledge M Muhler and his group of the chair of Technical Chemistry at RUB for applying the catalyst onto the dielectric sheets.


## ORCID iDs

Sebastian Dzikowski  <https://orcid.org/0000-0001-5036-6770>

Ronan Michaud  <https://orcid.org/0000-0001-6432-052X>

Remi Dussart  <https://orcid.org/0000-0003-2001-5034>

Marc Böke  <https://orcid.org/0000-0003-1062-5808>

Volker Schulz-von der Gathen  <https://orcid.org/0000-0002-7182-3253>

## References

- [1] Becker K H, Schoenbach K H and Eden J G 2006 *J. Phys. D: Appl. Phys.* **39** R55–70
- [2] Koutsospyros A, Yin S M, Christodoulatos C and Becker K 2004 *Int. J. Mass Spectrom.* **233** 305–15
- [3] van Durme J, Dewulf J, Leys C and van Langenhove H 2008 *Appl. Catal. B Environ.* **78** 324–33
- [4] Zhang Y R, van Laer K, Neyts E C and Bogaerts A 2016 *Appl. Catal. B Environ.* **185** 56–67
- [5] Hensel K, Katsura S and Mizuno A 2005 *IEEE Trans. Plasma Sci.* **33** 574–5
- [6] Eden J G, Park S J and Kim K S 2006 *Plasma Sources Sci. Technol.* **15** S67–73
- [7] Allmen P V, Sadler D J, Jensen C, Ostrom N P, McCain S T, Vojak B A and Eden J G 2003 *Appl. Phys. Lett.* **82** 4447–9
- [8] Kim S O and Eden J G 2005 *IEEE Photon. Technol. Lett.* **17** 1543–5
- [9] Park S J, Kim K S and Eden J G 2005 *Appl. Phys. Lett.* **86** 221501
- [10] Eden J G et al 2003 *J. Phys. D: Appl. Phys.* **36** 2869–77
- [11] Dussart R et al 2010 *Eur. Phys. J. D* **60** 601–8
- [12] Kulsreshath M K, Golda J, Felix V, Schulz-von der Gathen V and Dussart R 2014 *J. Phys. D: Appl. Phys.* **47** 335202
- [13] Bryant P M, Clarke G C B, Kim T, Park S J, Eden J G and Bradley J W 2008 *IEEE Trans. Plasma Sci.* **36** 1248
- [14] Boettner H, Waskoenig J, O’Connell D, Kim T L, Tchertchian P A, Winter J and Schulz-von der Gathen V 2010 *J. Phys. D: Appl. Phys.* **43** 124010
- [15] Kushner M J 2004 *J. Appl. Phys.* **95** 846–59
- [16] Wollny A, Hemke T, Gebhardt M, Brinkmann R P and Mussenbrock T 2011 *IEEE Trans. Plasma Sci.* **39** 2684–5
- [17] Kulsreshath M K, Golda J, Schulz-von der Gathen V and Dussart R 2014 *Plasma Sources Sci. Technol.* **23** 045012
- [18] Golda J, Kulsreshath M, Boettner H, Felix V, Dussart R and Schulz-von der Gathen V 2014 *IEEE Trans. Plasma Sci.* **42** 2646–7
- [19] Chen F F 2006 Introduction to Plasma Physics and Controlled Fusion (*Plasma Physics, 2nd edn* vol 1) ed F F Chen (New York: Springer US)
- [20] Iseni S, Michaud R, Lefauchaux P, Sretenović G B, Schulz-von der Gathen V and Dussart R 2019 *Plasma Sources Sci. Technol.* **28** 065003
- [21] Pack J L, Voshall R E, Phelps A V and Kline L 1992 *J. Appl. Phys.* **71** 5363–71
- [22] Chicheportiche A, Lepetit B, Benhenni M, Gadea F X and Yousfi M 2014 *J. Phys. B: At. Mol. Opt. Phys.* **46** 065201
- [23] Eden J G and Park S J 2005 *Plasma Phys. Control. Fusion* **47** B83
- [24] Park S J, Chen J, Liu C and Eden J G 2001 *Appl. Phys. Lett.* **78** 419–21
- [25] Massines F, Gherardi N, Naudé N and Ségur P 2009 *Eur. Phys. J. Appl. Phys.* **47** 22805
- [26] Kulsreshath M K, Schwaederle L, Overzet L J, Lefauchaux P, Ladroue J, Tillocher T, Aubry O, Woytasik M, Schelcher G and Dussart R 2012 *J. Phys. D: Appl. Phys.* **45** 285202
- [27] Waskoenig J, O’Connell D, Schulz-von der Gathen V, Winter J, Park S J and Eden J G 2008 *Appl. Phys. Lett.* **92** 101503
- [28] Wollny A, Hemke T, Gebhardt M, Peter Brinkmann R, Boettner H, Winter J, Schulz-von der Gathen V, Xiong Z, Kushner M J and Mussenbrock T 2011 *Appl. Phys. Lett.* **99** 141504
- [29] Baragiola R A, Alonso E V, Ferron J and Oliva-Florio A 1979 *Surface Sci.* **90** 240–55
- [30] Avci M and Yamacli S 2010 *Math. Comput. Modell.* **51** 908–14